

Shell formation and two-dimensional nanofriction in three-dimensional ion Coulomb crystals

L. A. Rüffert¹ and T. E. Mehlstäubler^{1, 2, 3}

¹Physikalisch-Technische Bundesanstalt, Bundesallee 100, Braunschweig, 38116, Germany

²Institut für Quantenoptik, Leibniz Universität Hannover, Welfengarten 1, Hannover, 30167, Germany

³Laboratorium für Nano- und Quantenengineering,

Leibniz Universität Hannover, Schneiderberg 39, Hannover, 30167, Germany

(Dated: December 4, 2025)

Self-organized three-dimensional (3D) ion Coulomb crystals in linear Paul traps naturally form concentric shells that provide a curved, atomically resolved interface for studying two-dimensional (2D) nanofriction. Building on prior work that used 2D ion crystals to investigate one-dimensional (1D) nanofriction and orientational melting, we leverage this foundation to extend friction studies from linear ion chains and planar rings to 3D shell structures. Using molecular-dynamics simulations, we first map shell formation as a function of ion number N and the trapping aspect ratio, yielding a simple relation that can aid ion-number estimation in experiments. We compute a Peierls–Nabarro-type energy landscape for the rotation of the outer shell against the inner core, showing drastic changes in the effective energy barrier up to a factor of about 60 with only small changes in N . Using dynamical simulations, we apply rotational torques to the outer shell of selected systems and show that small changes in N impact the commensurability between shells and can, in some cases, induce a hysteretic response due to torque-induced metastable states. We find that spatially varying coupling to the inner-core corrugation can create coexisting fast and slow moving domains within the rotating outer shell, realizing multidimensional friction where intra-shell shear and inter-shell nanofriction act simultaneously. Our results have implications for stabilizing many-body systems and for the development of ultra-low-friction nanomechanical devices such as ion-based nanorotors and torque sensors.

I. INTRODUCTION

Dry friction is a fundamental phenomenon that governs interactions across scales, from nanotribology to macroscale systems. Frictional losses due to tribological contacts account for nearly a quarter of global energy consumption and impact key industrial sectors such as transportation, power generation, and manufacturing [1]. Understanding and controlling friction at the nanoscale is therefore of great importance. Various methods have been developed to investigate nanoscale friction, including atomic force microscopy (AFM) [2–4], tribological studies of two-dimensional (2D) materials like graphene [5–7], and model-friction experiments with trapped ions and colloids in optical lattices [8–11].

Trapped Coulomb crystals in Penning and Paul traps offer a powerful platform for studying nanofriction in highly controllable environments. These systems are used across various fields, including quantum computing [12–14], precision spectroscopy [15–19], and fundamental studies of quantum many-body phenomena [20–23]. Beyond these applications, the dynamics of large three-dimensional ion Coulomb crystals and strongly coupled non-neutral plasmas have been investigated extensively, establishing these systems as model platforms for collective dynamics and transport in the strongly coupled regime [19, 24–27].

The static properties of ion Coulomb crystals have been widely studied. As particle number increases, the system forms concentric ring- or shell-like structures in 2D and 3D geometries, respectively [28–33]. Recent work

has investigated orientational melting in 2D crystals with up to 15 ions, interpreted as thermally activated rotation of the outer ion ring around the central core [34]. For specific ion numbers (“magic numbers”), this rotation is hindered due to increased energy barriers, suppressing orientational melting. On a similar note, studies on the Wigner crystallization of 2D electron clusters showed a strong dependence on the solid-to-liquid phase transition on the particle number [35, 36].

In this work we use molecular dynamics simulations to show how the number of shells scales with the particle number and trapping ratios and deduce a power-law scaling allowing simple estimations of ion numbers in experimental settings (Conclusion A). We then treat rotating shells in the view of nanofriction and calculate a Peierls–Nabarro-type potential of the outer shell rotation over the corrugation potential formed by the inner shells. We find that the commensurability between the shells strongly affects the energy barrier for shell rotation, whose magnitude can change by up to a factor of about 60 when the ion number is varied by only one or a few ions (Conclusion B). When applying rotational torques to investigate dynamical friction between shells, we find that the depinning thresholds of the outer shell qualitatively follow the energy barriers obtained in Conclusion B. For some configurations, the driven system exhibits a hysteretic response due to torque-induced metastable states. Moreover, certain systems reveal a non-uniform distribution of the angular velocity along the rotation axis, leading to 1D friction between ion segments within the rotating 2D shell and giving rise to complex, multi-

dimensional friction phenomena (Conclusion C).

Our findings help to identify the mechanisms that result in a higher resilience to rotation of the outer shell which enhances the crystal stability against orientational melting, finding possible applications in multi-ion clocks [15, 16], quantum simulators [21, 37] and ion spectroscopy experiments [17, 18]. Conversely, structures with a low potential barrier for shell rotation might be of interest in the design of ultra-low-friction nanomechanical systems, such as ion-based nanorotors, gyroscopes or ultrasensitive torque detectors [38–41].

The paper is structured as follows: In Sec. II we first give an overview about the trapping of laser-cooled ions in a harmonic ion trap and the resulting self-organized Coulomb crystals, their shell structures in 3D configurations as well as an introduction over the different models of nanofriction.

Following this, we outline our simulation methodology in Sec. III and discuss our results in Sec. IV, first by analyzing shell formation and its dependence on the particle number and trapping potential.

In Sec. IV B, we calculate a Peierls-Nabarro-type potential of the outer shell rotation over the corrugation potential of the static inner shell.

Using our findings, we apply a range of external torques to the outer shell of selected configurations and use the resulting angular velocity to identify different dynamical friction regimes. These results are presented in Sec. IV C.

Finally, we discuss possible experimental realizations of our findings in Sec. V and summarize the main results of this study in Sec. VI.

II. THEORETICAL BACKGROUND

A. Ion Coulomb crystals

Ions which are being trapped in a Paul or Penning trap and are laser-cooled to a few mK form self-organized Coulomb crystals [24]. In a Paul trap, a rapidly oscillating rf electric field generates an average confining force on the ions that, in the ponderomotive approximation, is described by a time-independent quadratic potential in all three spatial directions [42].

We consider N identical ions with positions $\vec{r}_i = (x_i, y_i, z_i)$, mass m , and charge Q , interacting via the Coulomb force. Approximating the rf-potential to be harmonic, the total potential energy of the system can be written as

$$\mathcal{V} = \sum_i \frac{m}{2} (\omega_x^2 x_i^2 + \omega_y^2 y_i^2 + \omega_z^2 z_i^2) + \sum_{i < j} \frac{Q^2}{4\pi\epsilon_0 d_{ij}}, \quad (1)$$

where ϵ_0 is the vacuum permittivity and $d_{ij} = |\vec{r}_i - \vec{r}_j|$ the distance between ions i and j . The secular frequencies ω_x , ω_y , and ω_z define the confinement strength in each direction and thus the overall shape of the ion crystal.

We define the axial direction (along which only static fields are applied) as the z -axis, and the radial direction in the xy -plane, so that the secular frequencies follow:

$$\begin{aligned} \omega_z^2 &= \frac{Q}{m} u_{\text{DC}}, \\ \frac{\omega_{x/y}^2}{\omega_z^2} &= \frac{1}{2} \frac{Q}{m} \frac{u_{\text{rf}}^2}{u_{\text{DC}} \Omega_{\text{rf}}^2} - \frac{1}{2} \mp c_{xy}. \end{aligned} \quad (2)$$

Here, u_{DC} and u_{rf} are the static and oscillating field gradients, Ω_{rf} is the rf drive frequency, and c_{xy} accounts for anisotropies of the radial directions.

At zero temperature, the ions form a stable configuration determined by the balance between Coulomb repulsion and the confining potential. By adjusting the trap frequencies, the shape of the resulting crystal and the distances between the ions can be tuned. In this work, we focus on spheroidal crystals, defined by

$$\omega_z \leq \omega_r, \quad (3)$$

with degenerate radial frequencies $\omega_r = \omega_{x,y}$, which allows the overall geometry to be characterized by the aspect ratio

$$\alpha = \omega_r^2 / \omega_z^2. \quad (4)$$

For $\alpha > 1$, the crystal elongates along the z -axis and compresses in the radial direction [43].

B. Shell formation in self-organized Coulomb crystals

The emergence of shell structures in ion Coulomb crystals has been demonstrated both theoretically and experimentally on many occasions: Simulations with up to several thousand ions have been performed under symmetric trapping conditions ($\omega_x = \omega_y = \omega_z$) [44–46], while the shell formation in infinitely long, cylindrically confined Coulomb systems has been studied analytically [29]. Monte Carlo simulations revealed that the dimensionless linear particle density

$$\lambda = \sigma a / Q, \quad (5)$$

where σ is the linear charge density and a the Wigner-Seitz radius, determines the number of shells in such systems. The number of shells approximately follows the empirical relation

$$N_s \approx 0.78 \sqrt{\lambda} \quad (6)$$

for infinitely long Coulomb crystals. Experiments in ring-shaped traps have confirmed this scaling behavior [47]. However, Coulomb crystals confined in linear Paul traps always exhibit finite boundaries along the axial direction of the trap. Figure 1 shows an experimental image of a 3D Coulomb crystal consisting of approximately 200 $^{172}\text{Yb}^+$ ions in a Paul trap, forming two distinct shells.

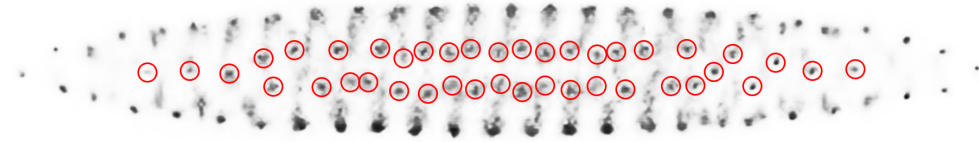


FIG. 1: Experimental image of a three-dimensional (3D), Doppler-cooled Coulomb crystal of approximately 200 $^{172}\text{Yb}^+$ ions taken with an EMCCD camera. The aspect ratio of the trapping potential is $\alpha \approx 9$. The crystal consists of an inner shell (ions highlighted in red) and a helix shaped outer shell, which wraps around the inner structure.

The inner shell ions are highlighted in red, and the trapping potential has an aspect ratio of $\alpha \approx 9$.

In very large Coulomb crystals with prolate spheroidal shapes, the number of shells also approximately follows Eq. (6) [31]. However, whether this scaling holds for smaller systems and varying values of α remains an open question. Our study finds a reasonable agreement with Eq. (6) albeit with a slightly higher prefactor of $N_s = 0.83\sqrt{\lambda}$ for finite crystals. Although many studies have explored how the overall crystal shape depends on the ratio of the trapping potential [33, 43], less attention has been paid to how the number of shells scales with α . The scaling of the number of shells with ion number and α will be discussed in the results section.

C. Nanofriction

Two of the most widely used theoretical models to describe nanoscale friction are the Prandtl-Tomlinson (PT) and the Frenkel-Kontorova (FK) model. Both of which provide key insights into atomic-scale friction.

PT model: single particle dynamics

The PT model [48, 49] describes a single point mass, such as an Atomic Force Microscope (AFM) tip, moving over a periodic potential representing a crystal surface. A spring connects the tip to a carrier moving at constant speed. The energy of the system is made up of the periodic interaction potential and the elastic energy of the spring. This setup leads to stick-slip motion, where the tip remains trapped in local minima until the spring force exceeds a threshold, causing a sudden jump of the tip over the corrugation barrier, which is characteristic of nanoscale friction.

FK model: many-body dynamics

The FK model [50] extends the concept of a single particle on a periodic potential to a chain of harmonically coupled particles interacting with a periodic substrate. Originally developed to describe crystal dislocations, it also serves as a model for friction on the nanoscale. A key prediction is the emergence of superlubricity, where static friction vanishes when the lattice constants of the two interacting surfaces form an irrational ratio. In this

case, no well-defined energy minima exist, allowing near-frictionless sliding [51, 52].

Experimentally, such Aubry-type transitions have been demonstrated in well-controlled systems such as ion Coulomb crystals in rf Paul traps, 2D colloidal monolayers and also a self-organized crystal [10, 11, 53, 54]. The Aubry transition is characterized by a sharp, well-defined change between a pinned and a smooth sliding state in ordered, incommensurate systems.

In contrast, stick-slip motion in most real-world scenarios, gradually evolves into smooth sliding as the driving velocity increases or the coupling between frictional layers is reduced [55–57].

C1. 1D nanofriction

External corrugation potential

The Frenkel-Kontorova (FK) model can be emulated by moving a linear ion chain across an optical lattice, which acts as a static corrugation potential [8, 9, 58, 59]. In this configuration, the ions are displaced via static electric fields while the lattice remains fixed. However, this setup only approximates realistic nanocontacts, where mutual interactions between atomic layers lead to deformations and backaction of the corrugation potential.

Interacting ion chains

Kiethe et al. [10, 53] demonstrated that Aubry-type transitions, soft modes and Hull functions can also be identified in self-organized systems of Coulomb crystals where the friction is caused by interacting ion chains. The work experimentally verified a sliding-to-pinning Aubry-type transition in a system with two adjacent ion chains, where a topological defect induced an incommensurability between the chains. The system is sketched in Fig. 2(a). The defect and the finite size of the system lead to a symmetry breaking at a critical corrugation strength, controlled via the radial trapping potential. The transition marks the boundary between a sliding and a pinned state in self-organized systems.

Duca et al. [34] investigated orientational melting between adjacent ion rings and found that the energy barrier for relative rotation diminishes for certain ion numbers. To demonstrate that these results are fully connected to the concept of 1D nanofriction, we perform a

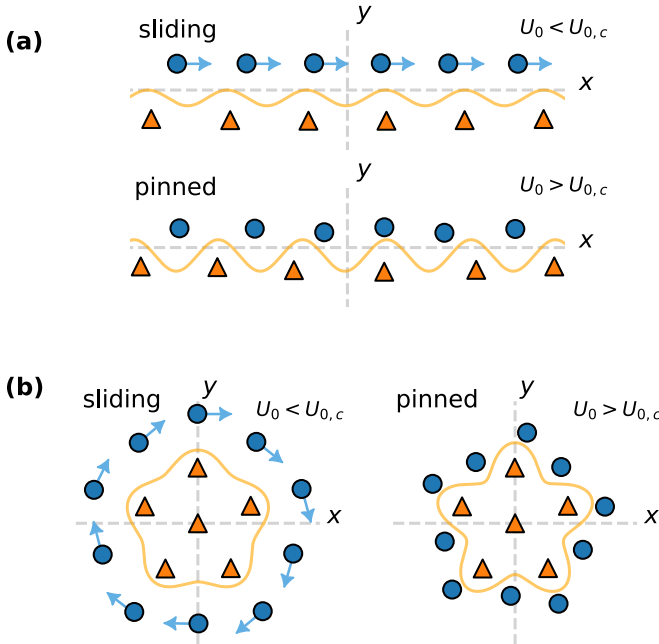


FIG. 2: Illustrative example of one-dimensional (1D) nanofriction in neighboring ion chains. Ion positions are represented by blue circles and orange triangles. The substrate potential (orange line) created by the triangular-marked ions induces a corrugation, which resists the sliding motion of the blue ion chain. Arrows indicate the motion lateral to the corrugation layer. The corrugation depth U_0 determines the transition from a pinned state to a free sliding state. (a) Adjacent ion chains with different periodicities. A similar setup was experimentally realized using a topological defect in [10] to verify an Aubry-type transition from sliding to pinning when the corrugation depth U_0 exceeds a critical value $U_{0,c}$. (b) Ring configuration of two adjacent ion chains. The number of ions directly dictates the periodicity between the two chains and therefore the commensurability. A similar system was used by Duca et al. to investigate orientational melting in 2D Coulomb crystals [34]. We simulate the pinned state by fixing the positions of the corrugation ions and increase the trapping potential, until the corrugation depth exceeds a critical value $U_{0,c}$, causing the system to be pinned.

proof-of-concept simulation by fixing the inner core of ions and changing the radial confinement. With this, we find an Aubry-type transition at a critical point, similar to the findings of Kiethe et al. [10, 53], depending on the commensurability as illustrated in Fig. 2(b).

C2. 2D Nanofriction

One way to extend the concept of 1D nanofriction in self-organized systems to 2D is by analyzing the frictional coupling between concentric crystal shells in 3D Coulomb

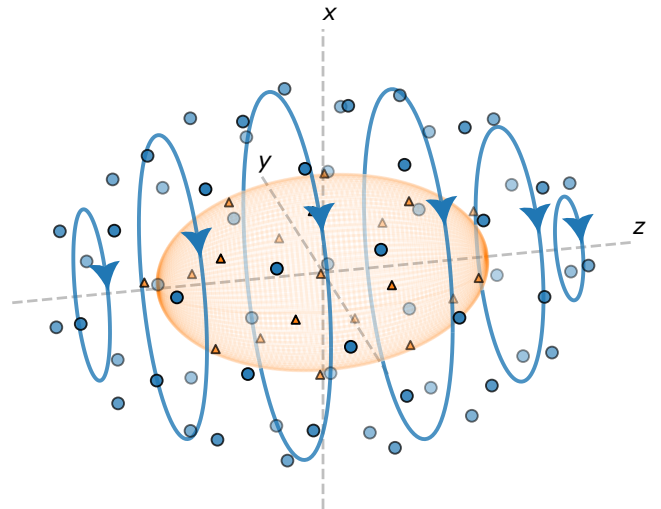


FIG. 3: Model system of two-dimensional (2D) nanofriction in a three-dimensional (3D) self-organized Coulomb crystal ($N = 80$) with two shells. Ions of the outer shell are represented by blue circles. Ions of the inner shell are shown as orange triangles. The ratio of the trapping frequencies is determined by $\omega_r > \omega_z$, causing the crystal to be of a spheroidal shape. The inner shell is approximated by a spheroidal surface (orange shade) for easier distinction of the two shells. The shear rotation around the z -axis of the outer shell is illustrated with blue circular arrows.

crystals, as shown in Fig. 3. The inner shell (orange triangles), approximated by an ellipsoidal surface, acts as a 2D corrugation potential for the outer shell (blue circles). When the outer shell rotates (blue arrows), lateral forces arise due to this corrugation, giving rise to 2D nanofriction.

In an ideal 2D system, ions form a hexagonal lattice which is the structural ground state of an infinite 2D ion crystals [33, 60]. When two such lattices interact, the Frenkel-Kontorova (FK) model can be extended to describe interlayer friction in two dimensions [61, 62]. In smaller crystals, however, curvature of the layers and lattice defects complicate theoretical modeling. We adopt a phenomenological approach and use molecular dynamics (MD) simulations to identify configurations that exhibit notably different frictional behavior despite having similar ion numbers.

III. METHODS

A. Molecular dynamics simulations and parameters

We describe the ion dynamics using the Langevin equation, which accounts for Brownian motion through a friction

tion term with coefficient η and stochastic forces $\vec{\epsilon}_i(t)$:

$$m_i \frac{d^2 \vec{r}_i}{dt^2} = -\frac{d}{d\vec{r}_i} \mathcal{V} - m_i \eta \frac{d\vec{r}_i}{dt} + \vec{\epsilon}_i(t). \quad (7)$$

The stochastic forces ensure thermal equilibrium at temperature T , with their correlation structure determined by the fluctuation-dissipation theorem. In experiments, these forces originate from photon absorption and spontaneous emission in laser cooling. For Doppler cooling, the maximum friction coefficient is $\eta \propto \hbar k^2$ and shows best agreement with experimental data for $\eta = (2.5 \dots 3.0) \times 10^{-21} \text{ kg s}^{-1}$ [63]. For finite temperatures, we simulate the system for several times the timescale η^{-1} to ensure thermalization. The kinetic energy serves as a consistency check for the target temperature.

After thermalization, we record ion positions and velocities for further analysis. The choice of time step must account for the oscillation frequencies of the chosen ion species. As a continuation of our previous work [23], we choose Be^+ with a mass of 9.01 amu as the primary ion species in our simulations, although the results presented in this study are independent of the chosen ion species. We choose a fixed axial secular frequency of $\omega_z/2\pi \approx 180 \text{ kHz}$ in all of the simulations. We find that setting the integration time step about a factor of 100 smaller than the fastest secular frequency in the simulated crystal sufficiently prevents numerical errors. The validity of the simulations have been verified using experimental results in previous work [23, 53, 63].

It should be noted that the frictional behavior generally depends on the interplay between Coulomb interactions and external confinement. Within our static-harmonic pseudopotential model, a uniform rescaling of all secular frequencies leaves the dimensionless dynamics unchanged. We therefore fix $\omega_z \approx 180 \text{ kHz}$ and vary the aspect ratio $\alpha = \omega_r^2/\omega_z^2$ and the ion number N , allowing us to explore structural rearrangements and their influence on friction.

Simulated annealing

To consistently prepare our crystals in the same structural state to ensure reproducible and comparable measurements, we employ a Simulated Annealing (SA) algorithm [64, 65] to find the structural ground state: we initialize the crystal with random ion positions at a high initial temperature in a molten state. By successively reducing the temperature, while logging the potential energy of the system, configurations of lower energy can be found. For each new temperature step, the system is initialized in the lowest energy state that has been found. This process is repeated until the temperature is set to 0. Multiple SA runs are executed until the same configuration has been found repeatedly, indicating that the structural ground state has been found. The complete algorithm is explained in more detail in Appendix A. While SA is a powerful algorithm to explore the energy landscape and reliably converges on low-energy config-

urations, it cannot guarantee that the true global minimum has been found. In this paper, we assume that repeated convergence to the same configuration across multiple SA runs serves as a practical proxy for having identified the structural ground state.

IV. RESULTS

First, we will present the findings of the structural properties of finite Coulomb crystals, specifically the scaling of the number of shells with the particle number N and the aspect ratio of the trapping potential α . We will then focus on the effective energy barrier for the outer-shell rotation which will give us indications on the dynamic friction regimes which we will investigate in the last subsection of the results.

A. Dependence of the number of shells on α and N

We examine the general formation of shell structures as a function of the particle number N and the aspect ratio of the trapping potential α . We define the point at which a new shell forms when the ion closest to the minimum of the trapping potential ($x = y = z = 0$) is displaced from the z -axis, meaning

$$x_i \neq 0 \wedge y_i \neq 0. \quad (8)$$

Therefore, a string of ions forming along z with $x = y = 0$ would not be counted as a new shell. However, to allow for an even more nuanced analysis, we will define systems for which the ion closest to the minimum of the trapping potential fulfills the condition

$$x_i = 0 \wedge y_i = 0, \quad (9)$$

as a linear-shell structure. This distinction will allow for more precise estimations of particle numbers, based on the found number of shells. The exact method we use to evaluate the number of shells from a given set of ion positions is detailed in the Appendix B.

The analysis is conducted over a broad parameter space, ranging from 1 to 800 ions and from aspect ratios of the trapping potential ranging from $\alpha = 1.0$ to 8.22. We calculate the structural ground state configuration for systems up to 100 ions. For systems $N > 100$ we add individual ions to the outer shell along the z -axis one at a time from alternating directions and let the system equilibrate to limit computation time. This will most likely result in metastable crystal configurations for $N > 100$ that are of higher energy than the ground state. While the number of shells could, in principle, vary between metastable states and the ground state, extended simulations showed that such discrepancies have no significant impact on the overall trends in shell formation. Therefore, the study of shell structures in relation to N

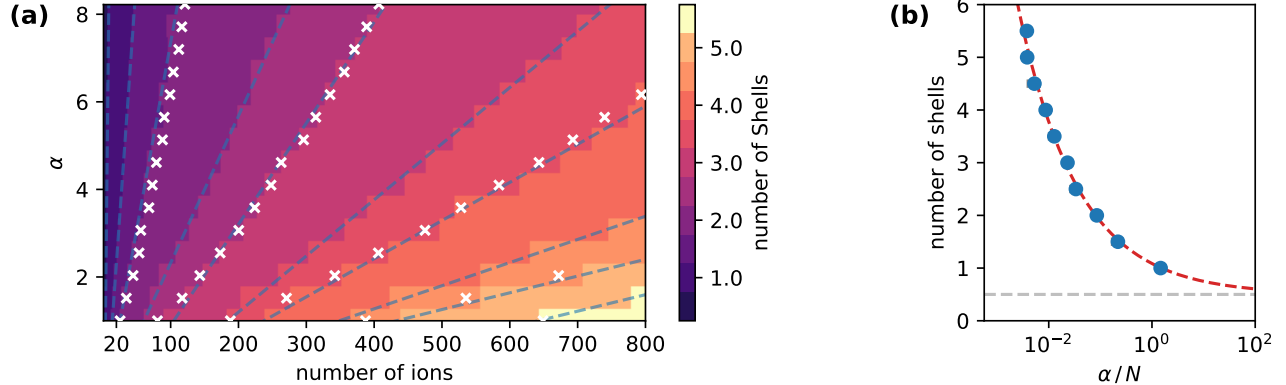


FIG. 4: (a) Number of shells as different colored regions with respect to the number of ions N and the aspect ratio of the trapping potential $\alpha = \omega_r^2/\omega_z^2$. A brighter color means a larger shell number. Half numbered shell counts describe crystals containing a linear chain of one or more ions on the z -axis. Linear fits to the transition regions are plotted as blue dashed lines. The white crosses mark the transition between full shell counts predicted by the linear particle density using $N_s = 0.83\sqrt{\lambda}$. (b) The number of shells is plotted with respect to the ratio between α/N . A power-law function was fitted to the data (red dashed line). Grey dashed line shows the limit of $N_s = 0.5$, which by definition represents the minimum achievable number of shells.

and α remains robust, even when metastable states are considered.

The findings of the analysis are given in Fig. 4(a), where we plot the number of shells in dependence on the number of ions and the ratio of the trapping potential α as a color gradient. A brighter color indicates a larger number of shells. We also include the linear-shells by counting them as half shells, based on the definition given above. We find a linear dependence of the transition regions between different numbers of shells on the number of ions and the aspect ratio of the trapping potential α . Linear fits to the transition regions are shown as blue dashed lines in Fig. 4(a). The slopes of these fits, which are the ratios of α/N , become increasingly shallow for larger shell counts.

To compare the results to the empiric predictions for infinite cylindrical Coulomb crystals (6), made by Hasse et al. [29], we estimate the linear density λ for each system: Assuming that the linear density for the finite systems is roughly constant around a range $|z| < \Delta z$, we can approximate λ by counting the number of particles within this range. Although the choice of Δz is somewhat arbitrary, values for $\Delta z = 0.1 L_z$ to $0.4 L_z$ have been tested, with L_z being the length of the crystal in the z -direction, without having a significant impact on the final results. We find that the shell transitions follow the empirical relation of

$$N_s \approx 0.83\sqrt{\lambda}, \quad (10)$$

highlighted as white crosses in Fig. 4(a), which is in good agreement with the empirical findings by Hasse et al. $N_s \approx 0.78\sqrt{\lambda}$. For systems with $\alpha \approx 1$ the linear density is slightly overestimated due to the more pronounced

curvature of the spheroid along z , resulting in a larger offset to this empirical relation. However, the estimation of the number of shells based on the linear density generally holds up for smaller spheroidal shaped crystals with finite boundaries. It is important to note that for fixed aspect ratio α , a uniform rescaling of all trap frequencies preserves the dimensionless linear charge density λ , which primarily determines the number of shells in the crystal. The observed shell configurations are therefore invariant under changes of the absolute trapping strength, as long as α is kept constant.

Following the results of Fig. 4(a), we find that the number of shells follows a power-law relation of

$$N_s \approx 0.6 \cdot \left(\frac{\alpha}{N}\right)^{-0.37} + 0.5, \quad (11)$$

which is shown as a red, dashed line in Fig. 4(b). The blue data points show the slopes α/N of the linear fits (blue dashed lines in Fig. 4(a)). To account for the fact, that the definition of the half-shell structure remains somewhat arbitrary, we apply an additional error estimate of 20% to the ratio of α/N for non-integer shell numbers. The curve approaches the limit value of 0.5, which by definition (9) represents the minimum achievable number of shells.

Since the number of shells can in general be easily identified by modern EMCCD imaging systems in Paul-trap experiments and the aspect ratio of the trapping potential is given by the applied dc- and rf-voltages, the number of ions in an experiment can be estimated by using relation (11).

Conclusion A

We mapped the number of shells versus ion number N

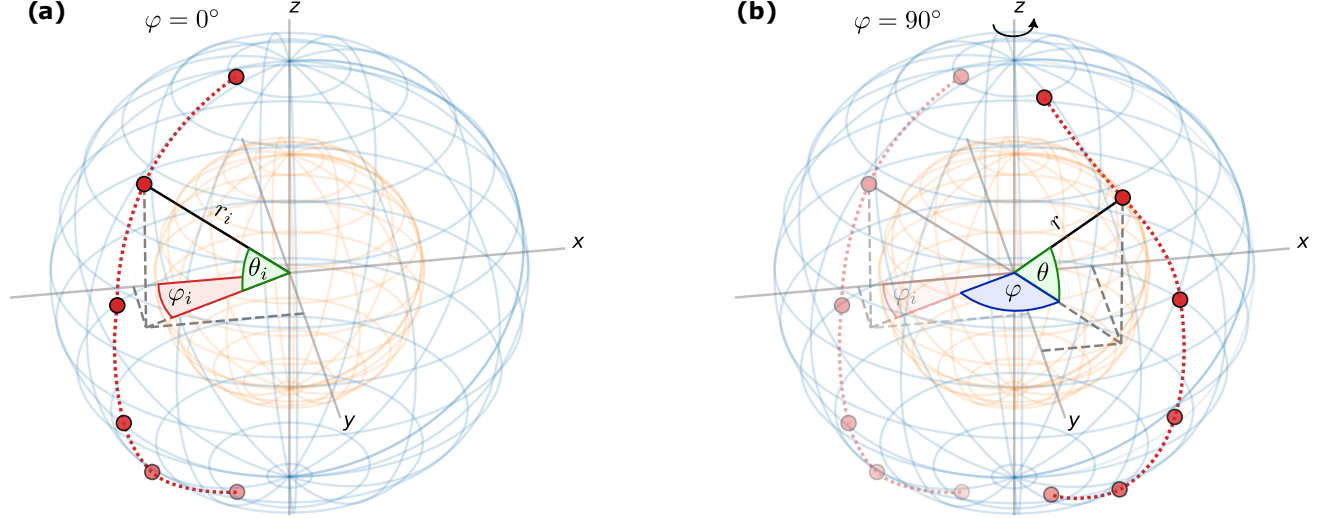


FIG. 5: Rotation of the outer shell (blue wireframe) around the z -axis for an $N = 80$ ion crystal with trapping aspect ratio $\alpha = 1$. Inner shells are shown in orange. For clarity, only the driving ions (red markers) are plotted explicitly and connected by a dashed red line for easier visualization. The position of each driving ion is described in spheroidal coordinates (r, θ, φ) , where φ is the azimuthal angle relevant for the rotation. (a) Initial configuration at $\varphi = 0^\circ$. The initial coordinates r_i , θ_i , and φ_i of a sample ion are shown in black, green, and red, respectively. (b) Configuration after rotation to $\varphi = 90^\circ$. The initial position (φ_i) is shown with reduced opacity for reference. The rotation angle φ is measured relative to φ_i and is identical for all driving ions. The outer shell is rotated by incrementally rotating the driving ions (red markers) around the z -axis in $\Delta\varphi = 1^\circ$ steps. While radial and polar motion is allowed during relaxation, for the driving ions, the azimuthal position is fixed during each rotation step. The dynamics of all other ions of the outer shell are unrestricted. The ions of the inner shells are kept static throughout the simulation.

and trap aspect ratio α and observe near-linear transition boundaries between different shell-regimes whose slopes α/N decrease with higher shell counts. We find that the transitions between shell numbers follows the local linear-density scaling $N_s \approx 0.83\sqrt{\lambda}$ (consistent with the results of Hasse et al. for infinite cylindrical Coulomb crystals), and we find a power-law scaling of the number of shells with the ratio α/N (see Eq. (11)). Since N_s is easily imaged and α is known experimentally, these relations enable a general upper and lower bound estimate of N in the experiment.

B. Energy barriers in rotating ion shells

The effective energy barrier provides direct insight into the frictional properties of sliding interfaces and can generally be defined as

$$E_{\text{eff}} = \max \Delta E(\vec{r}) = \max E(\vec{r}) - \min E(\vec{r}), \quad (12)$$

where $E(\vec{r})$ is the total potential energy at a given position \vec{r} . We compute E_{eff} for ground state configurations with up to 100 ions and selected trap aspect ratios $\alpha = (1, 1.52, 3.07, 4.10)$. Only crystals with at least two shells are considered ensuring inter-shell friction can occur.

To map the potential energy landscape, we rotate the outer shell around the z -axis in discrete steps of $\Delta\varphi = 1^\circ$ and measure the potential energy $E(\varphi)$. During this process, the inner shell remains fixed, enforcing a shear motion between the shells. To drive the outer shell while allowing for minimization of the potential energy at each step, we first determine a continuous ion chain between the z -poles of the crystal that will drive the rotation.

Fig. 5(a) shows the initial setup for a $N = 80$ ion crystal at $\alpha = 1.0$. The driving ions which form the shortest connected chain between the poles along the z -axis are highlighted as red circles. For clarity, we only show wireframe representations of the outer shell (blue) and the inner shell (orange). The position of each driving ion is given in spheroidal coordinates (r, θ, φ) , where φ is the azimuthal angle relevant for the rotation.

The initial configuration shown in Fig. 5(a) at $\varphi = 0^\circ$ defines the initial spheroidal coordinates r_i , θ_i , and φ_i . Fig. 5(b) shows the crystal after rotation of the outer shell to $\varphi = 90^\circ$. The rotation angle φ is measured relative to φ_i and the same angle φ is applied to all driving ions, which push the rest of the outer shell by Coulomb repulsion. After each $\Delta\varphi$ step, the system relaxes to a local energy minimum, with the driving ions fixed at φ , while all other outer shell ions are free to move. After relaxation, the total potential energy of the system

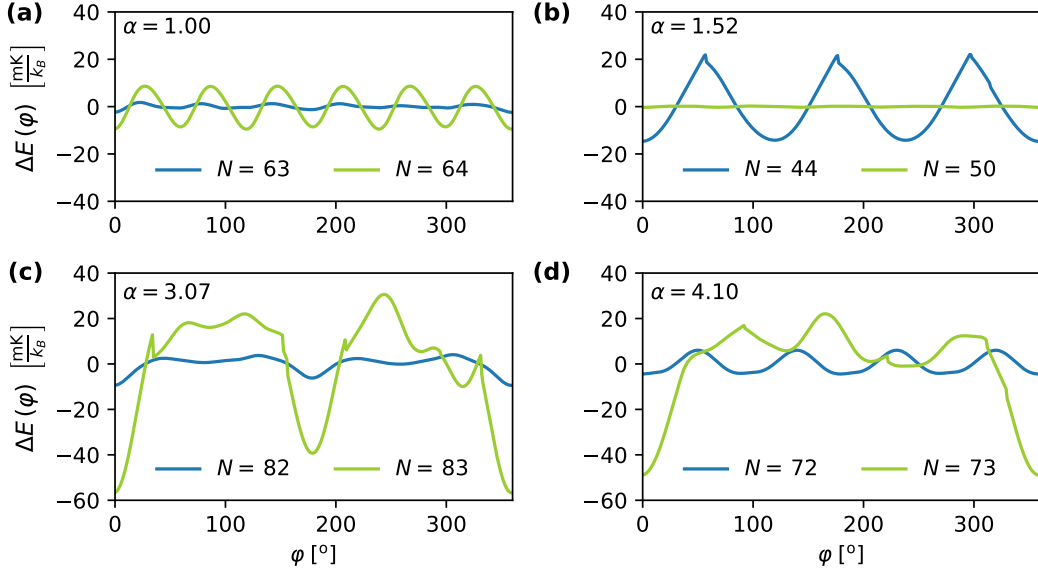


FIG. 6: Angle dependent modulations of the Peierls-Nabarro-type potential of the outer shell for selected crystal configurations. The ratio of the trapping potential $\alpha = (1.0, 1.52, 3.07, 4.10)$ is indicated in each plot. The inner shell ions are kept static throughout the rotation. Periodicities in the different graphs reflect the structure of the inner shell. Non-differentiable points in $\Delta E(\varphi)$ indicate a temporary rearrangement of the outer shell ions during the rotation. The systems were selected based on the significant change in the energy barriers while only slightly changing the particle numbers between the respective systems.

$E(\varphi + \Delta\varphi)$ is measured. The relaxed total energy $E(\varphi)$ plays the role of an effective Peierls–Nabarro-type (PN) potential of the rotational coordinate. Here the collective object is the entire outer shell treated as a rotated interface with fixed rotational angle φ for the set of driving ions, while all remaining degrees of freedom are relaxed under this constraint.

After a full rotation of 360° , we calculate the angle dependent energy difference

$$\Delta E(\varphi) = E(\varphi) - \langle E \rangle, \quad (13)$$

where $\langle E \rangle$ is the average of the total potential energy $E(\varphi)$ taken over the full 360° rotation. Examples of $\Delta E(\varphi)$ are shown for selected cases in Fig. 6. We specifically chose systems that show significant differences in the potential energy landscape while being similar in ion number.

The structure of the inner shells of the selected configurations is shown in the Appendix in Fig. 14, which provides a reference for the following discussion. The system $\alpha = 1.0, N = 64$ as well as $\alpha = 1.52, N = 44$ and $\alpha = 4.10, N = 72$ all exhibit periodic modulations in $E(\varphi)$ with periodicities of $60^\circ, 120^\circ$ and 90° , respectively. These reflect the inner shell symmetries: In the $\alpha = 1.0$ case the inner shell forms two hexagonal cells along the z -axis, causing a modulation of precisely 60° in $E(\varphi)$.

In the $\alpha = 1.52, N = 44$ case, the inner shell consists of two counter-rotated tetrahedra causing a 120° mod-

ulation. In the $\alpha = 4.10, N = 72$ system, the inner shell forms a double helix of 10 ions with 90° separation between ion pairs.

Systems with higher ion numbers at $\alpha = 3.07$ and $\alpha = 4.10$ show a series of non-differentiable points where $E(\varphi)$ abruptly changes its slope, indicating reordering of the outer shell during relaxation. Despite these reordering events, both systems return to their initial state after a full 360° rotation, as $E(0^\circ) = E(360^\circ)$. This symmetry is not always preserved, as later results will show.

The selected systems demonstrate that small changes in ion number can significantly alter $E(\varphi)$, even if the shell configuration is only slightly altered. For example, for the two $\alpha = 1.0$ systems as well as both $\alpha = 1.52$ systems, the respective inner shells remain unchanged between the different ion numbers, while only the outer shell is slightly reconfigured, causing increased incommensurability and a flattened energy landscape.

In the $\alpha = 3.07$ case, the $N = 83$ system contains two additional ions in the double-helix inner shell compared to $N = 82$, increasing its size and the commensurability between the shells. For $\alpha = 4.10$, the helical symmetry observed in the $N = 72$ crystal is broken by an added ion in the $N = 73$ system, distorting the periodicity in $E(\varphi)$ and raising the energy barrier for rotation. A more detailed analysis of the inner shell structures and their effects on the commensurability is given in Appendix C.

We define the effective energy barrier as the peak-to-peak variation of the quasi-static Peierls–Nabarro-type

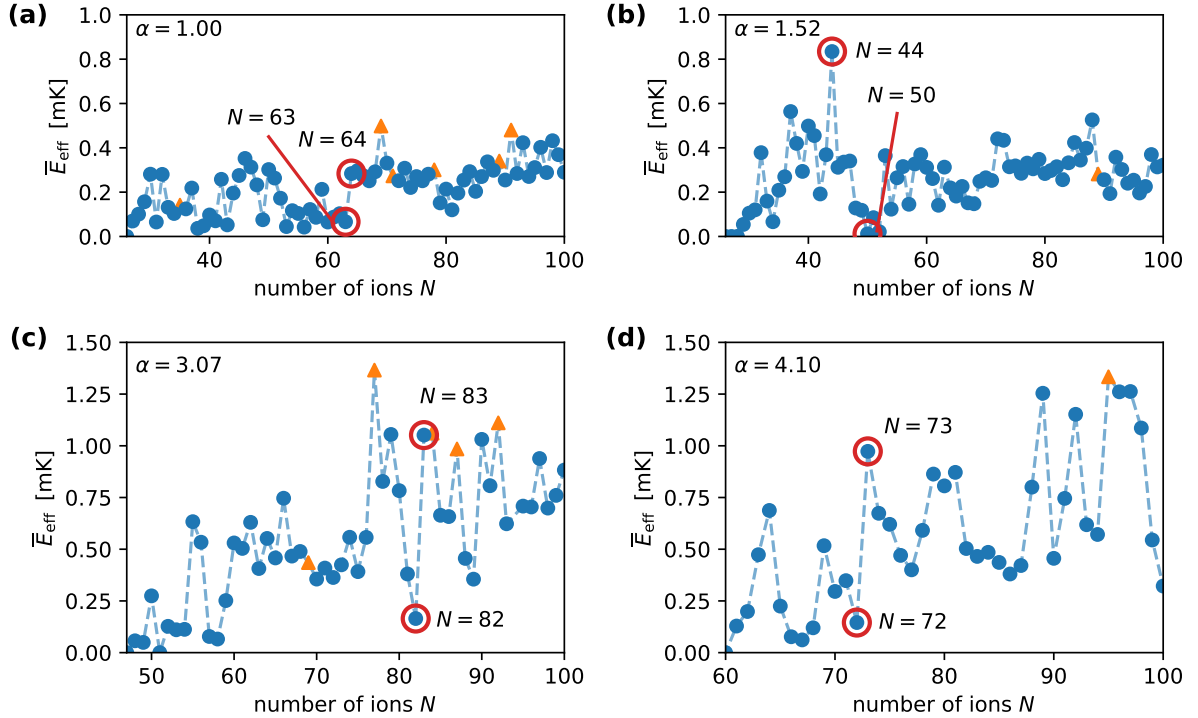


FIG. 7: Normalized effective energy barrier \bar{E}_{eff} for four selected ratios of the trapping potential $\alpha = (1.0, 1.52, 3.07, 4.10)$ plotted against the number of ions N . The ground state configuration was determined for each crystal. Selected configurations of interest are marked in red, where a large change in the effective energy is highlighted (corresponding to the Peierls-Nabarro-type potential in Fig. 6). Orange triangles mark systems that did not return to their initial configuration after a full rotation of the outer shell due to irreversible reordering of the ions. Note that configurations where the inner shell only consists of a single particle or a string of ions has been neglected due to an effective barrier of $E_{\text{eff}} = 0$.

energy landscape for the constrained rotation of the outer shell relative to the inner core,

$$E_{\text{eff}} = \max E(\varphi) - \min E(\varphi). \quad (14)$$

We normalize E_{eff} by the particle number N

$$\bar{E}_{\text{eff}} = E_{\text{eff}}/N \quad (15)$$

to account for an increase in potential energy with growing crystal size. We plot the results of \bar{E}_{eff} for crystal ground states up to $N = 100$ ions for trapping aspect ratios $\alpha = (1.0, 1.52, 3.07, 4.10)$ in Fig. 7. We only plot data for crystals with at least 2 shells. Orange triangles highlight configurations, where $E(0^\circ) \neq E(360^\circ)$ due to irreversible reordering in the outer shell.

We find distinct local minima and maxima in \bar{E}_{eff} for each system. The selected configurations of Fig. 6 are highlighted with red circles. We find, that the absolute value of the effective energy barrier changes by a factor of 4.35 in the highlighted $\alpha = 1.0$ systems, by a factor of 6.46 for $\alpha = 3.07$ and by a factor of 6.78 in the $\alpha = 4.10$ system while the ion number only changes by 1. In the

case for $\alpha = 1.52$, the change in the effective energy barrier is even more dramatic: here, the ion number differs by 6, resulting in a change of the effective energy barrier by a factor of 61.65.

Conclusion B

Our findings reveal a strong dependence of the spatial commensurability between the shells on the number of ions and the trap's aspect ratio α . Periodic features in the Peierls-Nabarro-type potential of the outer shell $E(\varphi)$ (see Fig. 6) are linked to highly symmetric inner shell structures, while abrupt changes or $E(0^\circ) \neq E(360^\circ)$ indicate rearrangements during rotation. Low effective energy barriers indicate the systems susceptibility to reduced friction between shells and therefore orientational melting. We identified systems where the effective energy barrier of the outer shell rotation changes by a factor of up to ~ 7 when changing the ion number N by 1 and up to ~ 62 when changing N by a few. In addition, certain configurations exhibit irreversible reordering of the outer shell during rotation, suggesting that these structures follow energetically favorable pathways that do not return to their initial configuration. Our findings demonstrate that small changes in crystal structure and

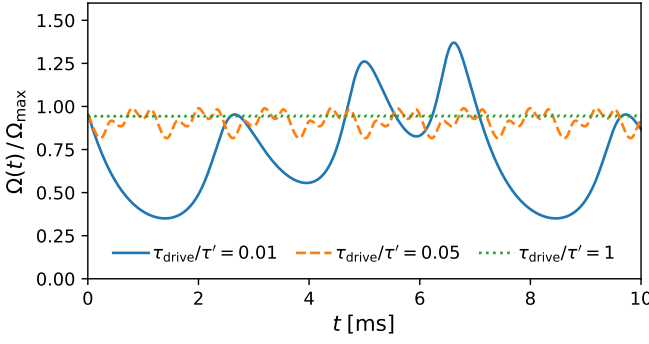


FIG. 8: Angular velocity $\Omega(t)$ of the outer shell over time, normalized by the maximum angular velocity Ω_{\max} achievable in the absence of corrugation-induced friction. The results shown are for the $N = 44$ system with an aspect ratio of the trapping potential of $\alpha = 1.52$. Results for three different driving torques are shown with the system being in a steady rotational state. Periodicities in the graphs indicate a full revolution of the outer shell. Oscillations indicate stick-slip motion caused by the corrugation potential. The average normalized angular velocity approaches 1 for increasing driving torques, showing a continuous transition towards the smooth sliding regime.

ion number can drastically alter the inter-shell potential barrier which has direct implications on the frictional behavior between shells.

C. Dynamical friction regimes

To investigate the inter-shell friction of the crystal configurations chosen in Sec. IV B, we apply a constant rotational torque to the outer shell and measure the resulting angular velocities, highlighting different frictional regimes and the dependence of the threshold-torque to initiate rotation on the ion number.

The simulations employ Langevin dynamics, accounting for both the corrugation-induced lateral torque from the inner shell and stochastic forces with damping representing laser cooling. As a result, the constant driving torque τ_{drive} must overcome both the corrugation torque τ_{corr} and the damping torque τ_{damp} to initiate rotation. Once the rotation has reached a steady state, it must follow that

$$\tau_{\text{drive}} + \langle \tau_{\text{damp}} \rangle + \langle \tau_{\text{corr}} \rangle = 0. \quad (16)$$

In the following results, we will normalize all values for the torque by the factor

$$\tau' = m_0 l_0^2 \omega_z^2, \quad (17)$$

where m_0 is the mass of the chosen ion species and l_0 is

the systems length scale defined as

$$l_0 = \frac{e}{\sqrt{4\pi\epsilon_0 m_0 \omega_z^2}}, \quad (18)$$

to allow for an easier comparison between the different systems.

To identify different frictional regimes, we will monitor the absolute value of the angular velocity Ω of the outer shell, given by

$$\Omega(t) = \frac{L(t)}{I(t)}, \quad (19)$$

where $L(t)$ denotes the time-dependent angular momentum and $I(t)$ the time-dependent moment of inertia of the outer shell.

Assuming steady-state balance between the applied torque and the damping torque due to laser cooling, the maximum angular velocity of the outer shell Ω_{\max} is given by

$$\Omega_{\max} = \frac{\tau_{\text{drive}}}{\eta \langle I \rangle}, \quad (20)$$

where η is the damping coefficient of the modeled laser cooling. Note, that while we use the time averaged value $\langle I \rangle$, slight fluctuations in position of the ions on the outer shell have negligible impact on the value of Ω_{\max} .

Fig. 8 shows $\Omega(t)/\Omega_{\max}$ over time, of the outer shell of the $\alpha = 1.52$, $N = 44$ configuration. Different driving torques are applied and the system is propagated until a steady state has been reached, before the data is recorded. The oscillations in $\Omega(t)/\Omega_{\max}$ are indicative of stick-slip motion, while the periodicities in the graphs reflect full revolutions of the outer shell. For increasing driving torques, the impact of the corrugation potential on the sliding velocity gradually diminishes, and the system approaches the smooth sliding regime.

We now normalize the time averaged angular velocity by the maximum angular velocity Ω_{\max} and define a sliding efficiency

$$S = \frac{\langle \Omega \rangle}{\Omega_{\max}}, \quad (21)$$

ranging from zero (pinned outer shell) to unity (smooth sliding) and will serve as the parameter to identify different sliding regimes.

We focus on the systems highlighted in Fig. 7 to analyze different frictional regimes and measure S for a wide range of applied driving torques. We find that for driving torques exceeding $\tau_{\text{drive}}/\tau' \approx 100$, the centrifugal forces on the outer shell can cause structural reordering. We therefore only apply driving torques, for which the crystal structure remains stable, ranging from $\tau_{\text{drive}}/\tau' = 10^{-4}$ to 100. The results of our friction analysis are presented in Fig. 9.

All data has been recorded with the system being in a stationary rotation state. If no ion on the outer shell

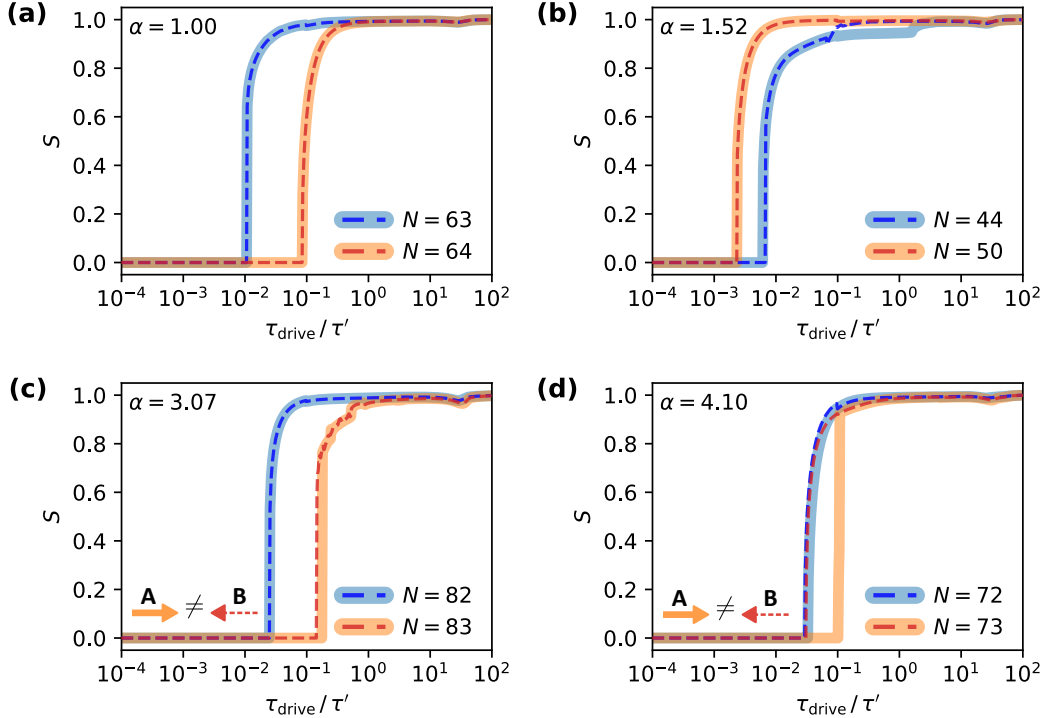


FIG. 9: Sliding efficiency S as a function of the driving torque for selected systems. The applied driving torque $\tau_{\text{drive}}/\tau'$ drives the rotation around the z -axis across the inner shells' corrugation potential. If none of the ions rotate by at least 1° within 10 ms, the average velocity is set to zero and the simulation is terminated. Solid lines (bright blue and orange) show the response for increasing torque, dashed lines (dark blue and red) for decreasing torque to emphasize hysteresis. At a critical point, the transition from pinning to stick-slip happens. At high torques, S asymptotically approaches 1, indicating smooth sliding. The hysteresis for the $N = 83$ system in (c) and the $N = 73$ system in (d) stems from a reconfiguration of the outer shell structure when the system is initialized at high driving torques. During the adiabatic down-sweep, the system ends up in a metastable configuration **B** that differs from the groundstate configuration **A** (directionality of the torque-sweep is indicated by the colored arrows). See main text for details.

has rotated by at least 1° within 10 ms, the simulation is canceled and S is set to 0. To investigate the systematic hysteresis, we also measured S at each driving torque by initializing the system with a maximum driving torque of $\tau_{\text{drive}}/\tau' = 100$ and adiabatically decrease the driving torque until a steady state has been reached at the target torque. The data for the hysteresis is plotted as dashed lines (blue and red) in Fig. 9.

For all systems, S exhibits a sharp onset, marking the transition from the pinned state to the stick-slip regime. The ordering of the depinning torques τ_{depin} , is qualitatively consistent with the effective energy barriers identified in Sec. IV B.

Conversely, the reverse sweep reveals a pinning transition at a characteristic torque τ_{pin} . The corresponding depinning and pinning thresholds for all systems are compiled in Table I. A comparison of the ratios of the depinning torques in the dynamic analysis and the torque ratios predicted from the static PN-energy landscape is given in Appendix D.

We find that for most systems, S asymptotically con-

α	N	$\tau_{\text{depin}}/\tau'$	τ_{pin}/τ'
1.00	63	0.011	0.011
1.00	64	0.085	0.085
1.52	44	0.006	0.007
1.52	50	0.002	0.002
3.07	82	0.025	0.025
3.07	83	0.181	0.142
4.10	72	0.033	0.030
4.10	73	0.104	0.031

TABLE I: Depinning and pinning torques for different values of α and particle numbers N . Standard errors of the given torques are below 2%.

verges to unity after τ_{depin} is exceeded. A second increase of S in the $\alpha = 1.52$, $N = 44$ and $\alpha = 3.07$, $N = 83$ systems stick-slip regime is attributed to a partial dynamical unlocking of previously more strongly pinned regions of the outer shell, increasing the overall sliding efficiency.

We observe a noticeable hysteresis in the $\alpha = 4.10$, $N = 73$ system which coincidentally falls in line with the

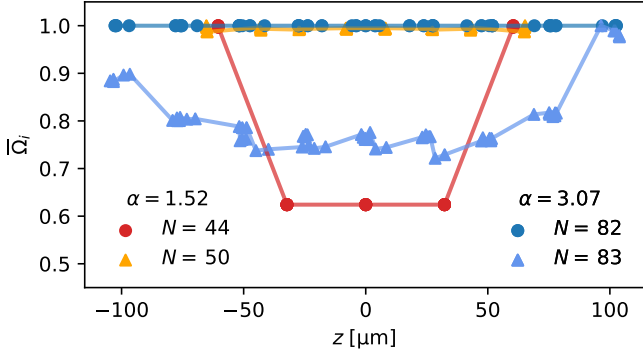


FIG. 10: Normalized average angular velocity of each outer shell ion, $\bar{\Omega}_i$, plotted versus the ions' z positions. For all data, the driving torque was chosen such that the outer shell sliding efficiency is $S = 0.9$ (see Fig. 9). Note, that ions lying close to the z -poles were excluded from this evaluation due to inconsistent values of $\bar{\Omega}_i$. We show the distributions only for $\alpha = 1.52$ and $\alpha = 3.07$, since the other cases ($\alpha = 1.0$ and $\alpha = 4.10$) yield nearly flat $\bar{\Omega}_i$ profiles for both ion numbers. For each pair of systems shown (differing only in ion number N), the z -dependence of $\bar{\Omega}_i$ is strongly N -dependent. This contrast arises from changes in inter-shell commensurability when N is varied (see main text for details).

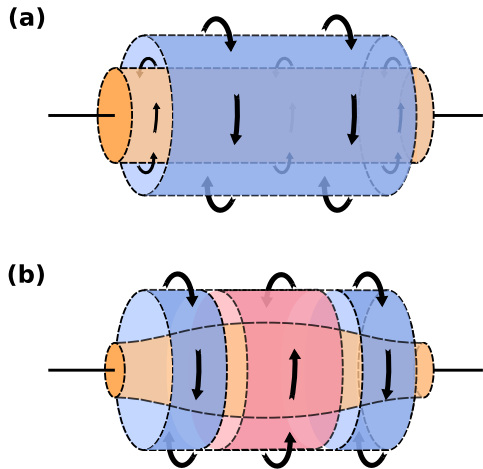


FIG. 11: Schematic illustration of multidimensional friction in a self-organized system. Domains of freely moving particles are indicated by shaded areas, while different colors denote regions with distinct shear motion that generate friction at their interfaces. (a) The orange-shaded inner cylindrical core acts as a two-dimensional corrugation potential for the blue-shaded outer shell. Shear motion between these two surfaces gives rise to 2D inter-shell friction. (b) Spatial variations in the coupling strength to the corrugation potential of the inner core (indicated by the varying shape of the inner orange corrugation) induce spatially different friction strengths for the outer shell. The resulting shear between domains within the outer shell (blue and red shaded areas) gives rise to 1D intra-shell friction.

sliding efficiency of the $N = 72$ system. Extended simulations show that, in the down-sweep, the outer shell relaxes into a metastable configuration that differs from the ground state, independent of the phase of the rotation. When initialized at high drive, the system follows a different path in configuration space and settles into a stationary rotational state with reduced corrugation. These lower-barrier states are dynamically accessible on the down-sweep but not when starting from the ground state configuration. We highlighted the differing configurations in Fig. 9(c) and (d) with **A** and **B** denoting the different crystal configurations and the arrows indicating the directionality of the torque-sweep. While a more detailed microscopic account of the geometric differences is beyond the scope of this work, our results indicate that the observed hysteresis originates from high-torque-induced rearrangements of the outer shell that reduce the effective angular corrugation and sustain rotation below the static depinning threshold. By contrast, in the other systems the absence of a comparable hysteresis suggests that such metastable states are either not realized or do not remain stable upon adiabatic deceleration.

Closer inspection of the high driving torque regime reveals a small local minimum in S at driving torques between $\tau_{\text{drive}}/\tau' \approx 25$ and 35 . While this feature is most pronounced in the $\alpha = 3.07$ systems, it consistently appears across all investigated configurations and points to a regime of enhanced energy dissipation.

A possible explanation is that, in this regime, the outer shell rotates at a frequency that aligns unfavorably with the periodicity of the corrugation potential, such that ions repeatedly encounter the flanks of the potential barriers in a dynamically inefficient phase. This leads to an increased energy loss and, consequently, to a reduction in S . Extended simulations showed a broadening of the angular velocity distribution within this range of driving torques, which supports the given explanation showing that some ions experience slightly different local barrier conditions and dynamical phases along their trajectory. Although this interpretation is consistent with the observed features, we note that the approximate alignment of the minima across systems with different corrugation periodicities suggests that additional collective or geometric effects may also play a role.

C1. Inter- and intra-shell friction

To quantify how the commensurability between the shells affects the homogeneity of the rotation in the self-organized outer shell, we compute the average angular velocity of each outer-shell ion and normalize it by the maximum particle value,

$$\bar{\Omega}_i = \frac{\langle \Omega_i \rangle}{\max(\langle \Omega_i \rangle)}. \quad (22)$$

For each system the driving torque is adjusted such that the shell sliding efficiency is $\bar{\Omega} = 0.9$, and $\bar{\Omega}_i$ is evaluated in the stationary rotating state. Ions located close to the z poles are omitted due to inconsistent values of $\bar{\Omega}_i$.

Figure 10 shows $\bar{\Omega}_i$ versus the ions' axial positions z_i for the $\alpha = 1.52$ and $\alpha = 3.07$ systems. The $\alpha = 1.0$ and $\alpha = 4.10$ cases are not shown since those systems yield near-flat profiles with $\bar{\Omega}_i \approx 1$ across z . Although the corrugation generally varies along z , a flat profile indicates that tangential Coulomb coupling within the outer shell redistributes corrugation-induced drag and homogenizes the particle speeds. By contrast, $\alpha = 1.52$, $N = 44$ and $\alpha = 3.07$, $N = 83$ show a reduction of $\bar{\Omega}_i$ toward the crystal center, whereas their partner systems ($N = 50$ and $N = 82$) remain homogeneous in $\bar{\Omega}_i$. Our results show that a change of N at the same α can lead to spatially different coupling strengths to the corrugation potential of the inner shell. When this localized friction dominates over intra-shell coupling, ring-like domains of different angular velocities develop within the outer shell creating an inhomogeneous velocity profile along z .

More broadly, self-organized systems driven across a static corrugation potential can realize coexisting fast and slow moving regions giving rise to 1D nanofriction that, together with the 2D inter-shell contribution, constitutes a multidimensional friction process. A schematic representation of this concept is shown in Fig. 11. A closer analysis of those inter- and intra-shell friction processes is beyond the scope of the present work and remains an interesting subject for future investigation.

Conclusion C

We identified distinct frictional regimes between shell structures in 3D Coulomb crystals, including pinned, stick-slip, and smooth sliding. The depinning torque and sliding efficiency strongly depends on ion number, the geometry of the inner shells and the aspect ratio of the trapping potential α . Our findings of τ_{depin} qualitatively match the expectations gained from the effective energy barriers calculated in Sec. IV B. The analysis of the systems dynamics have revealed a plethora of more complex inter-shell friction phenomena such as multidimensional friction, dynamical locking processes and differences in the hysteresis of the sliding velocity for different system sizes and values of α . While our findings offer only a first look into the dynamical interaction processes governing inter-shell friction, the observed dynamics point to a rich complexity which remains an interesting subject for future research.

V. PROSPECTS FOR EXPERIMENTAL REALIZATION

To experimentally observe the predicted ion-number dependence of the depinning threshold for the rotation of the outer shell, we propose preparing two crystals at fixed aspect ratio α that differ in shell commensurability and inner-shell occupancy, e.g. the $N = 72$ and $N = 73$

systems at $\alpha = 4.10$. These two systems are easily distinguishable on EMCCD images due to the additional ion in the inner shell of the $N = 73$ crystal compared to the $N = 72$ system. Preparation follows standard Doppler-annealing with repeated image-based state selection until the ground state configuration has been reached. Slightly lifting the radial degeneracy by a few percent ($\omega_x \lesssim \omega_y$) fixes the crystal orientation without significantly altering the inter-shell geometry and therefore the depinning threshold.

A key experimental concern is rf-induced micromotion (MM). In a linear Paul trap, the rf field drives motion at Ω_{rf} in the radial x - y plane. The local MM vector is aligned with $(x, -y)$, i.e. parallel to the rf quadrupole field. Therefore, ions located exactly on one of the radial axes experience purely radial MM, while ions at generic azimuthal positions acquire a finite tangential component which changes its direction in each quadrant so that the net rf drive along φ averages to zero over the full shell [66]. Thus, while individual ions do experience tangential MM, this does not by itself trigger the depinning of the outer shell. For our parameters (${}^9\text{Be}^+$, $\Omega_{\text{rf}} \approx 35$ MHz, $\omega_r/2\pi \approx 1.4$ MHz, $q_r \approx 0.186$), even the largest MM amplitudes at the outer shell (max. radius of ~ 36 μm) remain ~ 3 – 4 μm , well below the typical inter-ion spacing on the order of ~ 30 μm . Nonetheless, rf-induced micromotion enhances the coupling of residual electric-field noise to the secular modes and can heat the crystal [67], so an rf drive with high spectral purity and low noise will be required.

The relevant thermal budget is set by Doppler cooling versus residual heating in the secular modes and can be kept at the mK level with an axial cooling beam and standard excess-MM compensation.

Rotation of the outer shell can be triggered by applying a near-resonant push beam, slightly blue detuned from the dipole allowed cooling transition, e.g. 313 nm for Be^+ . By illuminating the outer rim ions, the push beam exerts a tangential radiation-pressure force on the outer shell. Assuming a perfectly tangential beam, the average radiation-pressure force per illuminated ion is

$$F_\varphi = \hbar k \Gamma_{\text{sc}}(\Delta, I) \quad (23)$$

with the scattering rate

$$\Gamma_{\text{sc}} = \frac{\Gamma}{2} \frac{s}{1 + s + (2\Delta/\Gamma)^2}, \quad (24)$$

where $s = I/I_{\text{sat}}$ is the saturation parameter, Δ the laser detuning and Γ the natural linewidth. The total torque created by the laser can be calculated by

$$\tau_{\text{L}}(I) = \sum_i r_i F_\varphi, \quad (25)$$

with the radial distances r_i of the ions to the z -axis. In the unsaturated limit ($s \ll 1$) one has $\Gamma_{\text{sc}} \propto I$, so the threshold intensity approximates the ratio of the depinning torques $I_{\text{th}}^{(N)}/I_{\text{th}}^{(N')}$ $\approx \tau_{\text{depin}}^{(N)}/\tau_{\text{depin}}^{(N')}$. For further

discussion on the ratio of the depinning torques, see Appendix D.

The rotation would then be visible by an azimuthal blurring of the outer-shell ion spots into short arcs or rings for longer exposures on the EMCCD images when the threshold intensity of the beam has been reached. For the $N = 72$ vs. $N = 73$ pair at $\alpha = 4.10$, our simulations predict a depinning-torque ratio on the order of ~ 4.1 , which should be observable as a comparable ratio of threshold intensities under otherwise identical conditions.

Finally, to suppress rigid-body rotation of the entire crystal, one may either use a second ion species of lighter mass to induce a pinning impurity (similar to Duca et al. [34]) or use differential laser forces on the inner and outer shell (similar to Kiethe et al. [10]) to keep the inner shell from rotating. In summary, reproducing the exact 3D ground state configurations is experimentally demanding, requiring imaging from two different angles, precise excess-micromotion compensation, and fine control of the secular anisotropy, but it is well within current ion-trapping capabilities and therefore technically feasible.

VI. SUMMARY

In this work, we investigated the emergence of shell structures and the frictional dynamics between concentric shells in 3D ion Coulomb crystals using molecular dynamics simulations. We systematically mapped out how the number of shells depends on both the particle number and the aspect ratio of the trapping potential, and derived a simple power-law scaling that may serve as a practical tool for estimating ion numbers in experiments.

Building on these structural insights, we analyzed the Peierls-Nabarro type energy landscape and calculated the effective energy barriers for outer shell rotation. We identified structural ground state configurations where minor changes in ion number significantly alter the frictional response: Our results reveal that spatial commensurability between adjacent shells strongly influences inter-shell friction, with certain configurations exhibiting reductions

in the effective energy barrier up to a factor of about 60 with only small changes in ion number. Similar sensitivity can also be observed in the dynamic frictional regimes under applied torques, where the onset of the pinning to sliding transition is again highly dependent on the commensurability between shells and therefore the number of ions. In addition, changes in the commensurability between shells can induce a hysteretic response due to torque-induced metastable states. Finally, we found a non-uniform angular velocity distribution of the outer shell particles when applying a rotational torque to the outer shell, caused by the axial dependence of the corrugation potential. This results in additional 1D nanofriction phenomena within the outer shell during the rotation and highlights the multidimensionality of inter-shell friction in self-organized systems.

Our findings highlight the sensitivity of inter-shell friction on the specific geometry and particle number and open pathways for precision control of nanofriction in synthetic systems. Future experimental efforts combining EMCCD imaging with a controlled ion number in Paul traps, could validate the strong dependence of inter-shell friction on the ion number by monitoring orientational melting dynamics of the outer shell. This could pave the way towards crystal configurations less prone to orientational melting and more advanced nanomechanical devices such as ion-based nanorotors or ultra-sensitive torque sensors.

ACKNOWLEDGMENTS

We would like to thank Ramil Nigmatullin for providing the basis of the simulation codes that were used during our research. We acknowledge support by the projects 18SIB05 ROCIT and 20FUN01 TSCAC. These projects have received funding from the EMPIR programme cofinanced by the Participating States and from the European Union's Horizon 2020 research and innovation programme. This project has been funded by the Deutsche Forschungsgemeinschaft (DFG, German Research Foundation) under Germany's Excellence Strategy – EXC-2123 QuantumFrontiers–390837967 and through CRC 1227 (DQ-mat), project A07.

[1] K. Holmberg and A. Erdemir, Influence of tribology on global energy consumption, costs and emissions, *Friction* **5**, 263 (2017).

[2] G. Binnig, C. F. Quate, and Ch. Gerber, Atomic Force Microscope, *Phys. Rev. Lett.* **56**, 930 (1986).

[3] Y. Martin, C. C. Williams, and H. K. Wickramasinghe, Atomic force microscope–force mapping and profiling on a sub 100-Å scale, *J. Appl. Phys.* **61**, 4723 (1987).

[4] C. M. Mate, G. M. McClelland, R. Erlandsson, and S. Chiang, Atomic-scale friction of a tungsten tip on a graphite surface, *Phys. Rev. Lett.* **59**, 1942 (1987).

[5] M. Dienwiebel, G. S. Verhoeven, N. Pradeep, J. W. M. Frenken, J. A. Heimberg, and H. W. Zandbergen, Superlubricity of Graphite, *Phys. Rev. Lett.* **92**, 126101 (2004).

[6] L. Xu, T.-B. Ma, Y.-Z. Hu, and H. Wang, Vanishing stick-slip friction in few-layer graphenes: The thickness effect, *Nanotechnology* **22**, 285708 (2011).

[7] D. Andersson and A. S. De Wijn, Understanding the friction of atomically thin layered materials, *Nat. Commun.* **11**, 420 (2020).

[8] D. Mandelli, A. Vanossi, and E. Tosatti, Stick-slip nanofriction in trapped cold ion chains, *Phys. Rev. B*

87, 195418 (2013).

[9] A. Bylinskii, D. Gangloff, and V. Vuletić, Tuning friction atom-by-atom in an ion-crystal simulator, *Science* **348**, 1115 (2015).

[10] J. Kiethe, R. Nigmatullin, T. Schmirander, D. Kalincev, and T. E. Mehlstäubler, Nanofriction and motion of topological defects in self-organized ion Coulomb crystals, *New J. Phys.* **20**, 123017 (2018).

[11] T. Brazda, A. Silva, N. Manini, A. Vanossi, R. Guerra, E. Tosatti, and C. Bechinger, Experimental Observation of the Aubry Transition in Two-Dimensional Colloidal Monolayers, *Phys. Rev. X* **8**, 011050 (2018).

[12] J. I. Cirac and P. Zoller, Quantum Computations with Cold Trapped Ions, *Phys. Rev. Lett.* **74**, 4091 (1995).

[13] R. Blatt and D. Wineland, Entangled states of trapped atomic ions, *Nature* **453**, 1008 (2008).

[14] C. Monroe and J. Kim, Scaling the Ion Trap Quantum Processor, *Science* **339**, 1164 (2013).

[15] K. Arnold, E. Hajiyev, E. Paez, C. H. Lee, M. D. Barrett, and J. Bollinger, Prospects for atomic clocks based on large ion crystals, *Phys. Rev. A* **92**, 032108 (2015).

[16] J. Keller, T. Burgermeister, D. Kalincev, J. Kiethe, and T. E. Mehlstäubler, Evaluation of trap-induced systematic frequency shifts for a multi-ion optical clock at the 10^{-19} level, *J. Phys. Conf. Ser.* **723**, 012027 (2016).

[17] J. Keller, H. N. Haussler, I. M. Richter, T. Nordmann, N. M. Bhatt, J. Kiethe, H. Liu, E. Benkler, B. Lipphardt, S. Dörscher, K. Stahl, J. Klose, C. Lisdat, M. Filzinger, N. Huntemann, E. Peik, and T. E. Mehlstäubler, High-accuracy multi-ion spectroscopy with mixed-species Coulomb crystals, *J. Phys. Conf. Ser.* **2889**, 012050 (2024).

[18] P. O. Schmidt, T. Rosenband, C. Langer, W. M. Itano, J. C. Bergquist, and D. J. Wineland, Spectroscopy Using Quantum Logic, *Science* **309**, 749 (2005).

[19] C. Champenois, M. Marciante, J. Pedregosa-Gutierrez, M. Houssin, M. Knoop, and M. Kajita, Ion ring in a linear multipole trap for optical frequency metrology, *Phys. Rev. A* **81**, 043410 (2010).

[20] R. Islam, E. Edwards, K. Kim, S. Korenblit, C. Noh, H. Carmichael, G.-D. Lin, L.-M. Duan, C.-C. Joseph Wang, J. Freericks, and C. Monroe, Onset of a quantum phase transition with a trapped ion quantum simulator, *Nat. Commun.* **2**, 377 (2011).

[21] J. W. Britton, B. C. Sawyer, A. C. Keith, C.-C. J. Wang, J. K. Freericks, H. Uys, M. J. Biercuk, and J. J. Bollinger, Engineered two-dimensional Ising interactions in a trapped-ion quantum simulator with hundreds of spins, *Nature* **484**, 489 (2012).

[22] J. G. Bohnet, B. C. Sawyer, J. W. Britton, M. L. Wall, A. M. Rey, M. Foss-Feig, and J. J. Bollinger, Quantum spin dynamics and entanglement generation with hundreds of trapped ions, *Science* **352**, 1297 (2016).

[23] L.-A. Rüffert, E. A. Dijck, L. Timm, J. R. C. López-Urrutia, and T. E. Mehlstäubler, Domain formation and structural stabilities in mixed-species Coulomb crystals induced by sympathetically cooled highly charged ions, *Phys. Rev. A* **110**, 063110 (2024).

[24] D. H. E. Dubin and T. M. O’Neil, Trapped nonneutral plasmas, liquids, and crystals (the thermal equilibrium states), *Rev. Mod. Phys.* **71**, 87 (1999).

[25] A. Poindron, J. Pedregosa-Gutierrez, and C. Champenois, Thermal bistability in laser-cooled trapped ions, *Phys. Rev. A* **104**, 043116 (2021).

[26] M. Baldovin, G. Vallet, G. Hagel, E. Trizac, and C. Champenois, Self-diffusion in a strongly coupled non-neutral plasma, *Phys. Rev. A* **109**, 043116 (2024).

[27] J. Zaris, W. Johnson, A. Shankar, J. J. Bollinger, and S. E. Parker, Numerical simulations of three-dimensional ion crystal dynamics in a penning trap using the fast multipole method, *J. Plasma Phys.* **91**, E53 (2025).

[28] S. L. Gilbert, J. J. Bollinger, and D. J. Wineland, Shell-Structure Phase of Magnetically Confined Strongly Coupled Plasmas, *Phys. Rev. Lett.* **60**, 2022 (1988).

[29] R. W. Hasse and J. P. Schiffer, The structure of the cylindrically confined Coulomb lattice, *Ann. Phys.* **203**, 419 (1990).

[30] R. W. Hasse and V. V. Avilov, Structure and Madelung energy of spherical Coulomb crystals, *Phys. Rev. A* **44**, 4506 (1991).

[31] M. Drewsen, C. Brodersen, L. Hornekær, J. S. Hangst, and J. P. Schiffer, Large Ion Crystals in a Linear Paul Trap, *Phys. Rev. Lett.* **81**, 2878 (1998).

[32] A. Radzvilavičius and E. Anisimovas, Topological defect motifs in two-dimensional Coulomb clusters, *J. Phys.: Condens. Matter* **23**, 385301 (2011).

[33] M. Drewsen, Ion Coulomb crystals, *Physica B* **460**, 105 (2015).

[34] L. Duca, N. Mizukami, E. Perego, M. Inguscio, and C. Sias, Orientational Melting in a Mesoscopic System of Charged Particles, *Phys. Rev. Lett.* **131**, 083602 (2023).

[35] M. Bonitz, V. Golubnichiy, A. Filinov, and Y. Lozovik, Single-electron control of Wigner crystallization, *Microelectron. Eng.* **63**, 141 (2002).

[36] V. Golubnichiy, P. Ludwig, A. Filinov, and M. Bonitz, Controlling intershell rotations in mesoscopic electron clusters, *Superlattices Microstruct.* **34**, 219 (2003).

[37] D. Kiesenhofer, H. Hainzer, A. Zhdanov, P. C. Holz, M. Bock, T. Ollikainen, and C. F. Roos, Controlling two-dimensional Coulomb crystals of more than 100 ions in a monolithic radio-frequency trap, *PRX Quantum* **4**, 020317 (2023).

[38] J. Ahn, Z. Xu, J. Bang, P. Ju, X. Gao, and T. Li, Ultrasensitive torque detection with an optically levitated nanorotor, *Nat. Nanotechnol.* **15**, 89 (2020).

[39] R. Ohira, T. Mukaiyama, and K. Toyoda, Breaking rotational symmetry in a trapped-ion quantum tunneling rotor, *Phys. Rev. A* **101**, 022106 (2020).

[40] J. Shao, W. Zhu, X. Zhang, and Y. Zheng, Molecular rotors with designed polar rotating groups possess mechanics-controllable wide-range rotational speed, *npj Comput. Mater.* **6**, 185 (2020).

[41] A. Singhania, S. Kalita, P. Chettri, and S. Ghosh, Accounts of applied molecular rotors and rotary motors: Recent advances, *Nanoscale Adv.* **5**, 3177 (2023).

[42] W. Paul, Electromagnetic traps for charged and neutral particles, *Rev. Mod. Phys.* **62**, 531 (1990).

[43] K. Okada, M. Wada, T. Takayanagi, S. Ohtani, and H. A. Schuessler, Characterization of ion Coulomb crystals in a linear Paul trap, *Phys. Rev. A* **81**, 013420 (2010).

[44] A. Rahman and J. P. Schiffer, Structure of a One-Component Plasma in an External Field: A Molecular-Dynamics Study of Particle Arrangement in a Heavy-Ion Storage Ring, *Phys. Rev. Lett.* **57**, 1133 (1986).

[45] H. Totsuji, Static and Dynamic Properties of Strongly-Coupled Classical One-Component Plasmas: Numerical Experiments on Supercooled Liquid State and Simulation of Ion Plasma in the Penning Trap, in *Strongly Coupled*

Plasma Physics, edited by F. J. Rogers and H. E. Dewitt (Springer US, Boston, MA, 1987) pp. 19–33.

[46] D. Dubin and T. O’Neil, Computer simulation of ion clouds in a Penning trap, *Phys. Rev. Lett.* **60**, 511 (1988).

[47] G. Birkl, S. Kassner, and H. Walther, Multiple-shell structures of laser-cooled $^{24}\text{Mg}^+$ ions in a quadrupole storage ring, *Nature* **357**, 310 (1992).

[48] L. Prandtl, Ein Gedankenmodell zur kinetischen Theorie der festen Körper, *Z. Angew. Math. Mech.* **8**, 85 (1928).

[49] G. A. Tomlinson, A molecular theory of friction, *Philos. Mag. Ser. 7* **7**, 905 (1929).

[50] Y. Frenkel and T. Kontorova, On the theory of plastic deformation and twinning, *Zh. Eksp. Teor. Fiz.* **8**, 1340 (1938), in Russian.

[51] S. Aubry, The New Concept of Transitions by Breaking of Analyticity in a Crystallographic Model, in *Solitons and Condensed Matter Physics*, Vol. 8, edited by M. Cardona, P. Fulde, H.-J. Queisser, A. R. Bishop, and T. Schneider (Springer Berlin Heidelberg, Berlin, Heidelberg, 1978) pp. 264–277.

[52] M. Peyrard and S. Aubry, Critical behaviour at the transition by breaking of analyticity in the discrete Frenkel–Kontorova model, *J. Phys. C: Solid State Phys.* **16**, 1593 (1983).

[53] J. Kiethe, R. Nigmatullin, D. Kalincev, T. Schmirander, and T. E. Mehlstäubler, Probing nanofriction and Aubry-type signatures in a finite self-organized system, *Nat. Commun.* **8**, 15364 (2017).

[54] D. A. Gangloff, A. Bylinskii, and V. Vuletić, Kinks and nanofriction: Structural phases in few-atom chains, *Phys. Rev. Res.* **2**, 013380 (2020).

[55] C. Voisin, F. Renard, and J.-R. Grasso, Long term friction: From stick-slip to stable sliding, *Geophys. Res. Lett.* **34** (2007).

[56] D. Gourdon and J. N. Israelachvili, Transitions between smooth and complex stick-slip sliding of surfaces, *Phys. Rev. E* **68**, 021602 (2003).

[57] C. Drummond and J. Israelachvili, Dynamic phase transitions in confined lubricant fluids under shear, *Phys. Rev. E* **63**, 041506 (2001).

[58] A. Benassi, A. Vanossi, and E. Tosatti, Nanofriction in cold ion traps, *Nat. Commun.* **2**, 236 (2011).

[59] Y. Braiman, J. Baumgarten, J. Jortner, and J. Klafter, Symmetry-breaking transition in finite Frenkel–Kontorova chains, *Phys. Rev. Lett.* **65**, 2398 (1990).

[60] D. H. E. Dubin, Theory of structural phase transitions in a trapped Coulomb crystal, *Phys. Rev. Lett.* **71**, 2753 (1993).

[61] J.-F. Han, B. Liu, and W.-S. Duan, The superlubricity of the special material with hexagonal symmetry in a two-dimensional Frenkel–Kontorova model, *Indian J. Phys.* **94**, 521 (2020).

[62] W. Cang-Long, D. Wen-Shan, Y. Yang, and C. Jian-Min, Application of Two-Dimensional Frenkel–Kontorova Model to Nanotribology, *Commun. Theor. Phys.* **54**, 112 (2010).

[63] K. Pyka, J. Keller, H. L. Partner, R. Nigmatullin, T. Burgermeister, D. M. Meier, K. Kuhlmann, A. Retzker, M. B. Plenio, W. H. Zurek, A. Del Campo, and T. E. Mehlstäubler, Topological defect formation and spontaneous symmetry breaking in ion Coulomb crystals, *Nat. Commun.* **4**, 2291 (2013).

[64] S. Kirkpatrick, C. D. Gelatt, and M. P. Vecchi, Optimization by Simulated Annealing, *Science* **220**, 671 (1983).

[65] S. Caracciolo, A. K. Hartmann, S. Kirkpatrick, and M. Weigel, Simulated annealing, optimization, searching for ground states (2023).

[66] D. J. Berkeland, J. D. Miller, J. C. Bergquist, W. M. Itano, and D. J. Wineland, Minimization of ion micro-motion in a Paul trap, *J. Appl. Phys.* **83**, 5025 (1998).

[67] D. Kalincev, L. S. Dreissen, A. P. Kulosa, C.-H. Yeh, H. A. Fürst, and T. E. Mehlstäubler, Motional heating of spatially extended ion crystals, *Quantum Sci. Technol.* **6**, 034003 (2021).

[68] J. Frausto-Solís, E. Liñán-García, and G. Santamaría-Bonfil, Tuned simulated annealing based on Boltzmann and Bose–Einstein distribution applied to MAXSAT problem, *J. Asian Sci. Res.* **4**, 14 (2014).

Appendix A: Simulated Annealing

To explore potential ground state configurations, we employ a simulated annealing (SA) algorithm [64, 65, 68] that iteratively reduces the system’s temperature, comparing the total potential energy after each temperature step to the previous one. If the new energy is lower than the previous one, the new configuration is accepted, and the temperature is reduced for the next step. If the energy is larger, the configuration is accepted with the probability

$$p_A = \min \left(1, \exp \left(-\frac{\Delta E}{k_B T} \right) \right), \quad (\text{A1})$$

where k_B is the Boltzmann-constant, T is the temperature and ΔE denotes the difference in energy between the previous temperature step and the current one. This process ensures that the system converges to a low-energy configuration, while allowing occasional transitions to higher energy states, thus exploring a broader energy landscape. To increase the likelihood of finding the ground state, multiple SA runs are performed in succession and starting positions of ions are systematically altered (e.g. by placing particles from the outer shell in the center of the crystal or vice versa). Only after finding the same minimum energy configuration repeatedly, the algorithm is stopped. Geometric symmetries in the crystal configurations can give a good indication of the validity of the ground state. For example, the inner shells of Coulomb crystals form different variants of deltahedral structures in the ground state, as illustrated in Fig. 12.

Appendix B: Shell Analysis

To characterize the shell structure of any given Coulomb crystal, we first fit a spheroid to the ion distribution. This fitting provides the semi-major axis a and the semi-minor axis b . Subsequently, we iteratively define an inner and an outer spheroidal shell with semi-axes

$$L_i^{\text{in}} = (i+1) \cdot \frac{s_{ab}}{a} \cdot d \quad (\text{B1})$$

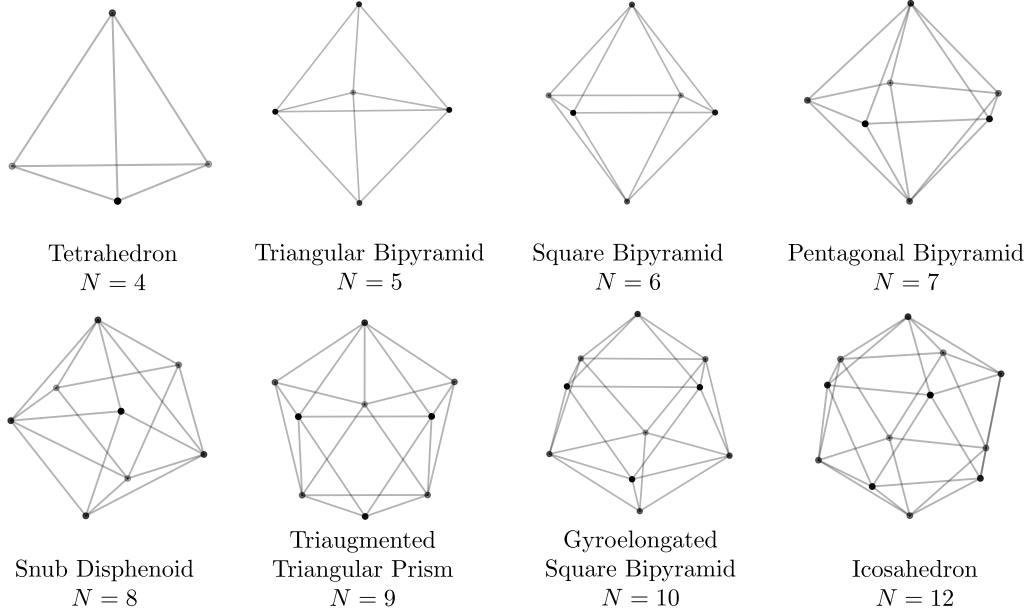


FIG. 12: Deltahedron shapes based on the ground states of ion crystals with trapping parameter $\alpha = 1$ for ion configurations up to $N = 12$. Note that the $N = 11$ configuration does not fit the definition of a deltahedron, which faces only consist of equilateral triangles. These shapes continue to appear in larger crystals when the innermost shells form.

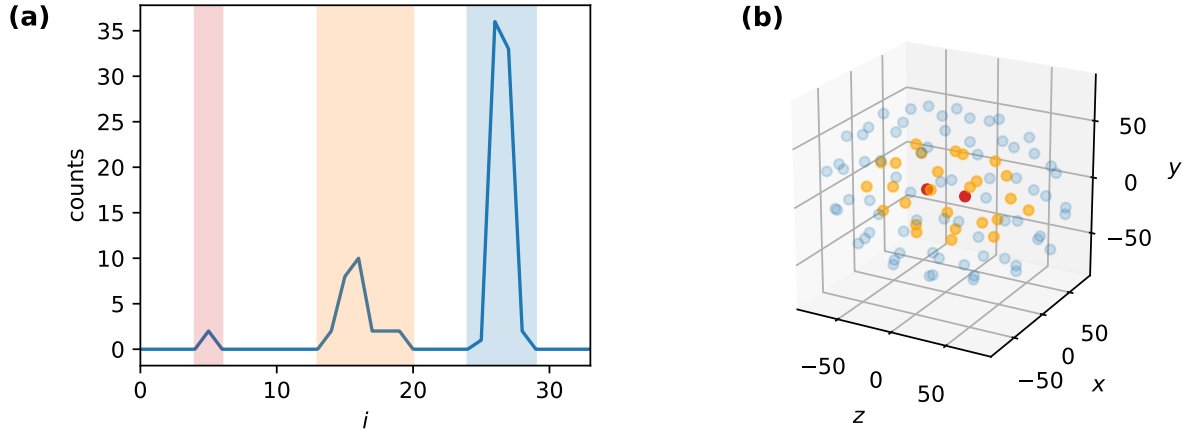


FIG. 13: (a) Histogram of a 100-ion crystal with the iteration variable i of the spheroidal shells (see eq. (B1) and (B2)). The spacing d was set to $2\text{ }\mu\text{m}$. The colored sections highlight the three shell regions. (b) 3D representation of the corresponding crystal. The color of the ions references the shell regions given in the histogram. The secular frequencies in the simulation are set to $\omega_{x,y,z}/2\pi = \{1.23, 1.23, 1\} \times 180\text{ kHz}$.

for the outer ellipsoid and

$$L_i^{\text{out}} = i \cdot \frac{s_{ab}}{a} \cdot d \quad (\text{B2})$$

for the inner ellipsoid, respectively. Here, i is an iteration variable that increases with each step, s_{ab} represents the respective semi-major or minor axes and d is the spacing between the two ellipsoidal shells.

In each iteration, we count the number of ions located between the inner and outer spheroids and compile these

counts into a histogram. This histogram reveals the shell structure of the crystal, providing insights into its spatial organization. This method is universally applicable to crystals with a spheroidal shape and ensures consistency across varying trap parameters. Fig. 13 shows an example of this shell analysis in the case of a crystal of 100 ions.

Appendix C: Influence of Shell Geometry on Commensurability and Friction

To better understand the change of incommensurability with ion number, we show the inner shell configurations for the systems analyzed in Sec. IV B in Fig. 14. For $\alpha = 1.0$ with $N = 63$ and $N = 64$, as well as for $\alpha = 1.52$ with $N = 44$ and $N = 50$, the inner shells are nearly identical, differing only by slight positional shifts. Therefore, we display only one representative configuration for each pair.

In general, ions constrained by the trapping potential minimize the potential energy by forming equilateral triangles. This leads to geometric structures that can be approximated by a gyroelongated hexagonal bipyramid for the two $\alpha = 1.0$ systems and a gyroelongated triangular bipyramid for both $\alpha = 1.52$ configurations. The characteristic exterior angles of these geometries are reflected in the periodicities of the total potential energy, provided the outer shell interlocks with the local minima of the corrugation potential, as seen in Fig. 6.

For the $\alpha = 3.07$ systems, the inner shell forms a double helix around the z -axis, with ion pairs which are equidistant to the z -axis and alternating in 90° steps in the xy -plane. Notably, adding a single ion increases the inner shell population by two.

In the $\alpha = 4.10$, $N = 72$ system, the inner shell also exhibits a helical structure that flattens into linear chains towards the edges. Adding one ion increases the inner shell count by one, causing a splitting of the alternating ion pairs along z and variation in their orientation within the xy -plane.

Changes in inter-shell friction with ion number can result from modifications to the inner shell, the outer shell, or both. In the $\alpha = 3.07$ and $\alpha = 4.10$ systems, the inner shells reconfigure with changing ion number, altering the inter-shell commensurability. In contrast, for $\alpha = 1.0$ and $\alpha = 1.52$, only the outer shell changes, while the inner shell remains structurally identical with only negligible shifts in the ion positions.

As shown previously in Fig. 6 and Sec. IV C, the $\alpha = 1.0$, $N = 63$ and $\alpha = 1.52$, $N = 50$ configurations exhibit a reduced effective energy barrier for outer shell rotation. To better understand the origin of these changes in commensurability, we plot the radial distance from the z -axis versus z for each ion in Fig. 15, focusing on the $\alpha = 1.0$, $N = 63$ and $N = 64$ as well as the $\alpha = 1.52$, $N = 44$ and $N = 50$ systems. We find that in both of these low-barrier systems, the ions are more evenly distributed along the z -axis compared to their high-barrier counterparts. This more homogeneous axial distribution increases the incommensurability between shells and thus reduces the effective energy barrier.

α	N, N'	$\tau_{\text{qs}}^N / \tau_{\text{qs}}^{N'}$	$\tau_{\text{dyn}}^N / \tau_{\text{dyn}}^{N'}$
1.00	64, 63	3.75	7.72
1.52	50, 44	26.74	3.00
3.07	82, 83	6.01	7.24
4.10	72, 73	4.10	3.15

TABLE II: Comparison of depinning-torque ratios for matched system pairs at fixed α . For each pair (N, N') , the ratio of the depinning torques of the quasistatic (qs) and in the dynamical (dyn) case is given. The quasistatic estimate is obtained from the maximum continuous slope of the Peierls-Nabarro-type $\Delta E(\varphi)$ calculated in Sec. IV B where the driving-ion chain is azimuthally constrained. The dynamic threshold (dyn) is extracted from unconstrained Langevin simulations of the outer shell with an applied rotational torque.

Appendix D: Discussion of depinning-torque ratios

From the energy landscape $\Delta E(\varphi)$ obtained in Sec. IV B, we estimate an upper bound for the minimal torque needed to initiate rotation by taking the maximum slope of the Peierls-Nabarro-type potential as the corrugation torque. Denoting this quasistatic estimate by τ_{qs}^N for a system with N ions, we define

$$\tau_{\text{qs}}^N = \max_{\varphi \in \mathcal{C}} \left| \frac{\partial \Delta E(\varphi)}{\partial \varphi} \right|, \quad (\text{D1})$$

where the set \mathcal{C} excludes angles at which discrete reordering events produce discontinuities in $\Delta E(\varphi)$. In Sec. IV C, we determine the dynamical depinning threshold τ_{dyn}^N from Langevin dynamics without constraining the degrees of freedom of the outer-shell ions. A concise comparison of the resulting ratios $\tau^N / \tau^{N'}$ between systems with the same trapping aspect ratio α is given in Tab. II. We find the quasistatic and the dynamic ratios differ by factors of up to 2.1 for systems that differ in ion number by just one and show a larger deviation by a factor of ~ 9 in the $\alpha = 1.52$ systems. These differences can be attributed to the azimuthal constraint that is applied to the driving ions in order to calculate the Peierls-Nabarro-type potential of the outer shell rotation in Sec. IV B. While in Sec. IV C, all outer-shell ions experience the same rotational torque without constraining the degrees of freedom. As a consequence, the outer shell can exploit small local rearrangements and take easier routes around the steepest parts of the corrugation landscape. Extended simulations show that in the dynamic case, after only a few degrees of rotation, the ion trajectories already deviate noticeably from the paths they take in the quasistatic case. Therefore, the ratios of the depinning-torques in the unrestricted rotation differs from the quasistatic case while the effect of the commensurability between the shells remains the deciding factor on which of the paired systems depins at lower driving torques.

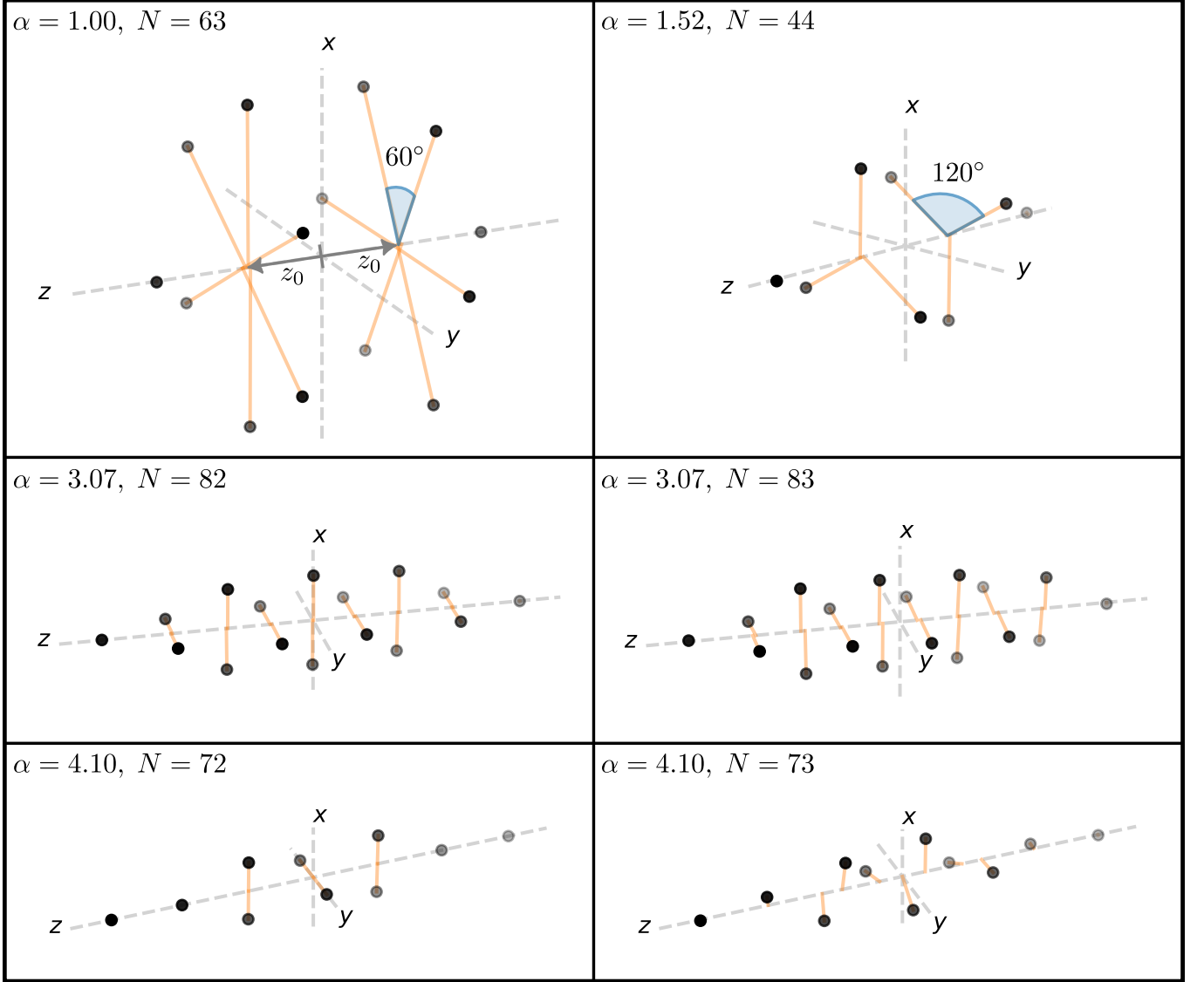


FIG. 14: Configurations of the inner shell ions for selected crystals. Orange lines mark the projection of the ion positions onto the z -axis, while the opacity of the ions decreases with distance from the viewer to aid spatial visualization. In the $\alpha = 1.0$ case, the ions positions can be approximated by the vertices of a gyroelongated hexagonal bipyramid, which consists of two parallel hexagons in the xy -plane, equally spaced from the origin by z_0 and rotated by 30° relative to each other. The exterior angle of 60° is highlighted in blue. A similar arrangement is found in the $\alpha = 1.52$ system, where the ions approximate a gyroelongated triangular bipyramid with an exterior angle of 120° . For $\alpha = 3.07$ and $\alpha = 4.10$, the inner shell structure depends on the ion number and generally takes the form of double helical arrangements along the z -axis. Except for the $\alpha = 4.10, N = 73$ case, the double helical structures consist of pairs of ions, equidistant to the z -axis and alternating in their rotation around z in steps of 90° . For the $\alpha = 4.10, N = 73$ system, this symmetry is broken due to an additional ion in the inner shell.

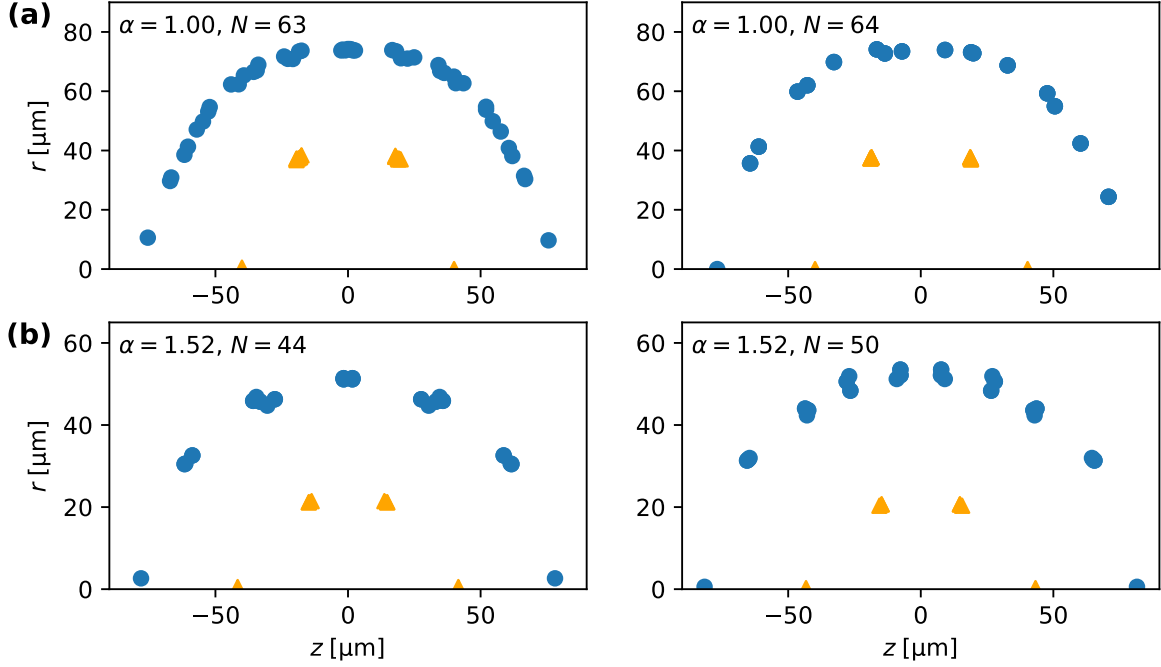


FIG. 15: Radial distance r from the z -axis plotted against the z position of each ion. Ions of the outer shell are shown as blue circles, ions of the inner shell as orange triangles. (a) For the $\alpha = 1.0$ crystal the ions distribute more homogeneously along the z -axis for the $N = 63$ case, compared to the $N = 64$ case, resulting in increased incommensurability and a reduced energy barrier for outer shell rotation. (b) In the $\alpha = 1.52$ case, the additional 6 ions cause a reconfiguration of the outer shell. Similar to the $\alpha = 1.0$ case, the more homogeneous distribution along z flattens the potential energy landscape due to increased incommensurability.